Research

Authors for correspondence:
Guofu Ma
e-mail: magf@nwnu.edu.cn
Ziqiang Lei
e-mail: leizq@nwnu.edu.cn

Nanostructure selenium compounds as pseudocapacitive electrodes for high-performance asymmetric supercapacitor

Guofu Ma[1], Fengting Hua[1], Kanjun Sun[2], Enke Fenga[1], Hui Peng[1], Zhiguo Zhang[1] and Ziqiang Lei[1]

[1]Key Laboratory of Eco-Environment-Related Polymer Materials of Ministry of Education, Key Laboratory of Polymer Materials of Gansu Province, College of Chemistry and Chemical Engineering, Northwest Normal University, Lanzhou 730070, People's Republic of China
[2]College of Chemistry and Environmental Science, Lanzhou City University, Lanzhou 730070, People's Republic of China

GM, 0000-0003-2142-0146

The electrochemical performance of an energy conversion and storage device like the supercapacitor mainly depends on the microstructure and morphology of the electrodes. In this paper, to improve the capacitance performance of the supercapacitor, the all-pseudocapacitive electrodes of lamella-like $Bi_{18}SeO_{29}/BiSe$ as the negative electrode and flower-like $Co_{0.85}Se$ nanosheets as the positive electrode are synthesized by using a facile low-temperature one-step hydrothermal method. The microstructures and morphology of the electrode materials are carefully characterized, and the capacitance performances are also tested. The $Bi_{18}SeO_{29}/BiSe$ and $Co_{0.85}Se$ have high specific capacitance ($471.3\,F\,g^{-1}$ and $255\,F\,g^{-1}$ at $0.5\,A\,g^{-1}$), high conductivity, outstanding cycling stability, as well as good rate capability. The assembled asymmetric supercapacitor completely based on the pseudocapacitive electrodes exhibits outstanding cycling stability (about 93% capacitance retention after 5000 cycles). Moreover, the devices exhibit high energy density of $24.2\,Wh\,kg^{-1}$ at a power density of $871.2\,W\,kg^{-1}$ in the voltage window of 0–1.6 V with 2 M KOH solution.

1. Introduction

Supercapacitors, prospective energy storage and conversion devices, have attracted tremendous interest due to the need for

power output devices for digital communications and electric vehicles owing to their facile manufacture, fast charging/discharge, long cycle life and higher power density than batteries [1–4]. Intrinsically, supercapacitors based on the principle of charge storage are divided into two types: pseudocapacitors and electric double-layer capacitors (EDLCs) [5]. In EDLCs, the charges are stored because of the surface adsorption of the ions from the electrolyte as a result of electrostatic attraction, thus forming two charged layers (double layer). Pseudocapacitors store charges by fast and reversible oxidation/reduction (Faradaic) reactions occurring at the electrode/electrolyte interfaces, as well as in the bulk near the surface of the electrode. Pseudocapacitors show higher capacitance when compared with EDLC-type devices due to the additional charge transferred within the defined potential [6–8].

Up to now, electrode materials with long cycle stability and high capacitance have obtained breakthrough progress, for instance transition metal sulfides (CuS [9], FeS [10], Al_2S_3 [11], etc.), transition metal oxides/hydroxides (NiO [12], ZnO [13], TiO_2 [14], $Co(OH)_2$ [15], $CoNi_2S_4$ [16], etc.) as well as conducting polymer materials (polyaniline [17], polypyrrole [18], etc.). The above electrode materials have been investigated for use in asymmetric supercapacitors extensively, due to their fast reversible redox reactions, cost-effectiveness, easy processability and relatively good cyclic stability [19]. However, compared with the transition metal dichalcogenide, the two-dimensional (2D) layered transition metal selenide has been paid less attention. The weak van der Waals force of 2D layered metal selenide is beneficial for insertion of guest species. Owing to their superior electronic structure and physical properties, the 2D nanosheet structural materials have attracted abundant attention compared to the corresponding bulk materials [20]. Recently, transition metal selenide has been shown to display outstanding electrochemical performance. Balasingam *et al.* have synthesized a few-layered $MoSe_2$ nanosheet by a simple hydrothermal method and further studied its electrochemical charge storage properties. It is shown that the $MoSe_2$ nanosheet electrode provides a symmetric device that exhibits $49.7\,F\,g^{-1}$ with a scan rate of $2\,mV\,s^{-1}$ and a largest specific capacitance of $198.9\,F\,g^{-1}$ [21]. Wang *et al.* made a flexible all-solid-state supercapacitor based on three-dimensional (3D) hierarchical $GeSe_2$ nanomaterials, which have a high specific capacitance of $300\,F\,g^{-1}$ at a current density of $1\,A\,g^{-1}$ [22]. Choi *et al.* synthesized $SnSe_2$ nanoplate–graphene composites and used them as a novel anode material for lithium ion batteries [23]. Tang *et al.* synthesized a new type of binder-free electrode material of NiSe/NF (NiSe nanowire film on nickel foam) by using the one-step hydrothermal method; it has a high specific capacitance of $1790\,F\,g^{-1}$ at a current density of $5\,A\,g^{-1}$ [24]. Yang *et al.* developed interconnected $Co_{0.85}Se$ nanomaterials on nickel foam directly through a facile single-step hydrothermal method, which exhibits a high specific capacitance of $1528\,F\,g^{-1}$ at $1\,A\,g^{-1}$ and excellent cycling stability [25]. Therefore, the transition metal selenide possesses outstanding electrochemical energy storage properties and deserves to be further investigated as an advanced electrode material for supercapacitor application.

In recent years, in order to improve energy density and power density to attain a win–win situation, researchers have assembled asymmetric supercapacitors (ASCs) with different electrode materials in aqueous electrolytes [26–30]. According to the literature, $E = 1/2CV^2$ (energy density formula); in order to improve energy density (E), two approaches can be used: maximizing the specific capacitance (C) and/or enlarging the operating potential window (V). Employing ionic liquids or organic electrolytes can increase the operating voltage effectively. However, their inherent deficiencies such as poor ionic conductivity and sometimes toxicity have hindered their practical application [26,27]. In comparison, an aqueous electrolyte is the best choice. The ASC is made up of two different electrodes, hence it is an essential prerequisite to select appropriate positive and negative electrode materials to assemble a high-performance ASC. Recently, the literature has depicted that the transition metal selenide has excellent electrochemical performance for a supercapacitor. But the synthesis of different selenium compounds as the positive and negative electrodes of a supercapacitor in the same system has not been well explored so far. In addition, the benzyl alcohol route in particular has been proved to be versatile for the synthesis of various metal oxide nanoparticles with good control over particle phase, size and shape [28,29]. The fact that the benzyl alcohol route is typically applied without the use of surfactants makes this approach ideal for mechanistic studies. Additives such as surfactants complicate the interpretation of the results due to their possible influence on nucleation and growth by complexation of cations [30,31]. Therefore, in a two-component system just consisting of a precursor and solvent, the complexity is decreased to a minimum, although benzyl alcohol itself may play multiple roles as reaction medium, oxygen source and/or capping agent. Another unique feature of non-aqueous systems is the possibility to monitor the organic reactions occurring in parallel to nanoparticle formation by standard analytical techniques. Thus, the use of benzyl alcohol as a solvent (without any template and surfactant) to synthesize transition metal selenium-based compounds is a very desirable route.

In this work, we have used a facile low-temperature one-step hydrothermal method without any template and surfactant (benzyl alcohol as the solvent) to synthesize two different transition metal selenides: $Bi_{18}SeO_{29}/BiSe$ and $Co_{0.85}Se$. The lamella-like $Bi_{18}SeO_{29}/BiSe$ and petal-like $Co_{0.85}Se$, which are used as negative and positive electrode materials, have high specific capacitance in aqueous electrolyte. The assembled ASCs possess excellent energy density and outstanding power density with a wide voltage window as well as high cycling stability in aqueous electrolyte.

2. Experimental

2.1. Materials

Bismuth nitrate pentahydrate ($Bi(NO_3)_3 \bullet 5H_2O$, Aladdin Industrial corporation, Shanghai, China), cobalt nitrate hexahydrate ($Co(NO_3)_2 \bullet 6H_2O$, Aladdin Industrial corporation, Shanghai, China), selenium oxide (SeO_2, Sitong Tianjin Chemical Reagent Co. Ltd, China) and benzyl alcohol (Aladdin Industrial corporation, Shanghai, China). All chemical reagents were of analytical grade and were not further purified before use.

2.2. Synthesis of $Bi_{18}SeO_{29}/BiSe$ nanocomposite

The $Bi_{18}SeO_{29}/BiSe$ nanocomposites were synthesized using the hydrothermal method in benzyl alcohol. In the typical process, $Bi(NO_3)_3 \bullet 5H_2O$ (0.582 g) and SeO_2 (0.111 g) were dispersed in benzyl alcohol solution (35 ml), stirring uniformly for 1 h with the assistance of ultrasonic vibration. After stirring vigorously at room temperature for about 10 min, the white solution was transferred to a 50 ml Teflon-lined stainless steel autoclave and heated at 180°C for 15 h. Finally, the resulting greyish precipitate was collected by centrifugation and on cooling to room temperature naturally. Subsequently, the greyish precipitate was washed with distilled water and ethanol several times to remove any possible ions and dried in a vacuum at 65°C overnight.

2.3. Synthesis of $Co_{0.85}Se$ nanomaterials

The cobaltous selenide ($Co_{0.85}Se$) nanosheets may also be synthesized by the hydrothermal method in benzyl alcohol solution; using 0.349 g $Co(NO_3)_2 \bullet 6H_2O$ and 0.111 g SeO_2 as raw materials, the process was similar to the synthesis of $Bi_{18}SeO_{29}/BiSe$ nanocomposites.

2.4. Materials characterization

The morphologies of $Bi_{18}SeO_{29}/BiSe$ and $Co_{0.85}Se$ were analysed using field emission scanning electron microscopy (SEM, Ultra Plus, Carl Zeiss) with a voltage of 5.0 kV. The microstructure of $Bi_{18}SeO_{29}/BiSe$ and $Co_{0.85}Se$ were further characterized by transmission electron microscopy (TEM, JEM-2010 Japan). The crystallographic structure of the materials was degassed at 200°C before nitrogen adsorption measurement. X-ray diffraction (XRD) was conducted using a Rigaku D/Max-2400 diffractometer, with Cu Ka radiation ($\lambda = 0.15418$ nm) at 40 kV and 100 mA. X-ray photoelectron spectroscopy (XPS) was performed using an Escalab 210 system (Germany). In the SEM, the elemental mapping of relative energy-dispersive X-ray spectrometry (EDS) was performed by a probe focused to 0.2 nm with a camera length of 20 cm.

2.5. Electrochemical measurements

2.5.1. Three-electrode system

The electrochemical performance of $Bi_{18}SeO_{29}/BiSe$ and $Co_{0.85}Se$ was studied in 2 M KOH solution using a three-electrode system. High-purity carbon rods and oxidation of saturated mercury electrode (Hg/HgO) were used as the counter electrode and the reference electrode, respectively. The working electrodes were manufactured as follows: in general, 80 wt% electrode materials (16.0 mg), 10 wt% commercial carbon black (acetylene black, 2.0 mg) as well as 10 wt% polymer binder (polyvinylidene fluoride, 2 mg) were mixed with some N-methyl-2-pyrrolidone to form a homogeneous slurry. Further, the obtained slurry was coated on nickel foam with an area of 1.0 cm^2 and dried at 65°C overnight, and

then weighed and pressed into sheets under 13 MPa to ensure adherence between the active materials and the current collector. The total mass of each electrode was limited to 3.0–5.0 mg [32].

2.5.2. Two-electrode system of asymmetric supercapacitors

The electrochemical measurements were further taken using a two-electrode system consisting of $Bi_{18}SeO_{29}$/BiSe and $Co_{0.85}Se$ electrodes in 2 M KOH electrolyte. The working electrodes of the two electrode system were fabricated similarly to the three electrodes. The as-prepared slurry was spread on the rounded nickel foam mesh current collector with an area of 1 cm^2 uniformly, and the coating was left in an oven at 65°C overnight. Afterwards, this was weighed and pressed into sheets under 13 MPa to ensure adherence between the active materials and the current collector. The total mass of each electrode was limited to 3.0–5.0 mg. Two different electrodes of the same or very close weight were selected for measurement.

Finally, the ASCs were assembled using lamella-like $Bi_{18}SeO_{29}$/BiSe as the negative electrode and flower-like $Co_{0.85}Se$ as the positive electrode with a separator (filter paper) and electrolyte solution; they were assembled into a sandwich cell construction (electrode/separator/electrode). To uniformly diffuse the KOH electrolyte solution into the pseudocapacitive material electrode, the separated and pseudocapacitive material electrodes were immersed in 2 M KOH electrolyte for 6 h and then assembled into the supercapacitor configuration.

2.6. Electrochemical testing

A CHI660D electrochemical workstation (Shanghai Chenghua Instrument Co. Ltd, China) was used in the three-electrode and two-electrode systems by cyclic voltammetry (CV), galvanostatic charge/discharge (GCD) and electrical impedance spectroscopy (EIS). The EIS measurement was measured at a frequency ranging from 10 mHz to 100 kHz with an impedance amplitude of ±5 mV in open circuit potentials. In addition, a LAND CT2001A cell tester (Wuhan Landian electronics Co. Ltd, China) with a computer controlled system was used for the cycle-life stability test.

In the three-electrode system, the gravimetric capacitances of the $Bi_{18}SeO_{29}$/BiSe or $Co_{0.85}Se$ sample were calculated from the charge–discharge curves based on the following equation:

$$C_s = \frac{I\Delta t}{m\Delta V}, \tag{2.1}$$

where C_s corresponds to the specific capacitance (F g^{-1}), I represents the discharge current (A), Δt represents the discharge time (s), m refers to the total mass (g) and ΔV refers to the voltage change (V) of the $Bi_{18}SeO_{29}$/BiSe or $Co_{0.85}Se$.

For the two-electrode cells of ASCs, it was calculated by the equation

$$Q = C_m \times \Delta V \times m. \tag{2.2}$$

To obtain $Q^+ = Q^-$, as well as to make use of the largest voltage window, the mass ratio of the positive and negative electrodes are acquired on the basis of the following equations [33]:

$$\frac{m^+}{m^-} = \frac{C_m^+ \times \Delta V^+}{C_m^- \times \Delta V^-}, \tag{2.3}$$

$$C_{cell} = \frac{I\Delta t}{m\Delta V}, \tag{2.4}$$

$$E = C_{cell}\Delta V^2 \times \frac{1000}{2 \times 3600} \tag{2.5}$$

and

$$P = E \times \frac{3600}{\Delta t}, \tag{2.6}$$

where C_m^+ and C_m^- are the specific capacitances (F g^{-1}), and ΔV^+ and ΔV^- represent the voltage ranges (V) of the $Co_{0.85}Se$ and $Bi_{18}SeO_{29}$/BiSe electrodes, respectively. C_{cell} denotes the specific capacitance (F g^{-1}) of the ASC device, I discharge current (A), Δt the discharge time, m the total weight (g) of the two electrodes, ΔV the voltage window (V), E (Wh kg^{-1}) the energy density and P (W kg^{-1}) the power density [34].

# 3. Results and discussion

3.1. Negative electrode

The purity and crystallinity of negative electrode $Bi_{18}SeO_{29}$/BiSe were investigated using powder XRD, as displayed in figure 1*a*; the peaks can be indexed to the hexagonal $Bi_{18}SeO_{29}$ phase (JCPDS card no. 42-0098) and the BiSe phase (JCPDS card no. 42-1045) from the XRD pattern. The strong diffraction peaks at 2θ angles of 27.77, 31.00, 32.74, 45.70, 46.97, 53.16, 55.45 and 57.34 could be readily indexed to the (221), (002), (400), (402), (440), (223), (621) and (442) planes of $Bi_{18}SeO_{29}$; the other diffraction peaks at 2θ angles of 19.16, 29.09, 39.98 and 43.28 can be indexed to the (005), (014), (108) and (110) planes of BiSe, respectively. The microstructure and morphology of $Bi_{18}SeO_{29}$/BiSe were investigated by SEM and TEM analyses. As indicated in figure 1*b*, the $Bi_{18}SeO_{29}$/BiSe exhibits a large amount of interconnected and ultrathin nanosheet structure. The high-resolution SEM image (figure 1*c*) gives a clear view of the nanosheets, consisting of abundant thin one-dimensional lamella-like structures which are well aligned together with intertwined nanosheet subunits; this can enable the easy flow and transfer of electrons and ions in the nanosheet structure. The unique structure of $Bi_{18}SeO_{29}$/BiSe can be further proved by TEM (figure 1*d*,*e*), in which are clearly displayed the thin layers with randomly intertwined nanosheet structure. Moreover, the high-resolution TEM image and the corresponding selected area electron diffraction (SAED), as described in figure 1*f*, demonstrate the polycrystalline nature of the nanosheets and illustrate clear lattice fringes, which can be assigned to the following crystal planes: 0.321 nm for $Bi_{18}SeO_{29}$ (221), 0.307 nm for BiSe (014) and 0.273 nm for $Bi_{18}SeO_{29}$ (400). A SAED image is displayed in figure 1*f* inset; the diffraction rings from inside to outside were indexed to the (221), (014), (108), (402) and (440) planes of the hexagonal $Bi_{18}SeO_{29}$/BiSe, which exhibits a crystalline characteristic. The clear lattice fringes and SAED are in agreement with the aforementioned XRD results. Although with some reservation, an approximate electrochemically active surface area was calculated from the Brunauer–Emmett–Teller method (BET) [35]. The BET surface area of the $Bi_{18}SeO_{29}$/BiSe is 19.35 $m^2\,g^{-1}$, as shown in figure 2*a*, which is similar to that of pure Co_3O_4 material (18.5 $m^2\,g^{-1}$) [36] and to that of emeraldine-di-hydrogen sulfate (22.1 $m^2\,g^{-1}$) [37]. The electrochemically active surface area can facilitate intercalation and de-intercalation of electrolyte ions.

To further confirm the chemical element compositions and the surface valence state information, $Bi_{18}SeO_{29}$/BiSe was evaluated by the XPS technique and EDS, as presented in figure 2. In the XPS survey spectrum of $Bi_{18}SeO_{29}$/BiSe, the elements of Bi, Se and O as well as C can be clearly identified (figure 2*b*). Figure 2*c* shows the high-resolution spectrum of the Bi 4f region, which exhibits two asymmetrical main signals corresponding to the deconvolution of Bi 4f7/2 (159.28 ± 0.3 eV) and Bi 4f5/2 (164.45 ± 0.3 eV) with a spin–orbit splitting of about 5.4 eV [38]. The binding energies of 159.28 eV and 164.45 eV can be attributed to the Bi^{3+} ion [39]. From the significant dispersion of the binding energy, it can be demonstrated that bismuth forms a mixture rather than pure metal oxide [40]. Further, the core-level spectrum of the Se 3d region is shown in figure 2*d*; the binding energy of 58.7 eV can be assigned to oxidized Se (SeO_X), which is in good agreement with previously reported values [30]. In addition, to verify the elemental distribution, $Bi_{18}SeO_{29}$/BiSe was further characterized by EDS (figure 2*e*); the corresponding element mapping images can unambiguously confirm the homogeneous distribution of bismuth, selenium and oxygen in the nanomaterial.

The electrochemical behaviour of $Bi_{18}SeO_{29}$/BiSe nanosheets was first studied by CV and GCD techniques with a three-electrode system in 2 mol l^{-1} KOH aqueous electrolyte. Figure 3*a* displays the CV curves of the $Bi_{18}SeO_{29}$/BiSe nanosheets as the negative electrode at different scan rates ranging from 5 to 30 mV s^{-1} in the potential window of -1 to 0 V. A pair of redox peaks can be clearly observed in the CV curves of the $Bi_{18}SeO_{29}$/BiSe composite at different scan rates, showing it has typical Faradaic pseudocapacitance behaviour. In detail, the oxidation peaks were seen in forward CV scans, while the reduction peaks were seen in the reverse CV scans. In highly alkaline solution, hydroxide ions are generated naturally, which are likely to gravitate towards the cathode at high potentials Thus, the reduction peak at 0.7 V corresponds to Bi^{3+} transformed into $Bi(OH)_2{}^+$ in the reduction process. The oxidation peaks at about -0.48 V and -0.35 V correspond to Bi^{3+}/Bi^0 transformation. Those peaks are also seen in some other studies [27,41,42]. It may be catalysed by the induction or oxidation of some unconverted Bi^0 during the reduction process, and the process has the following reaction [27,43]:
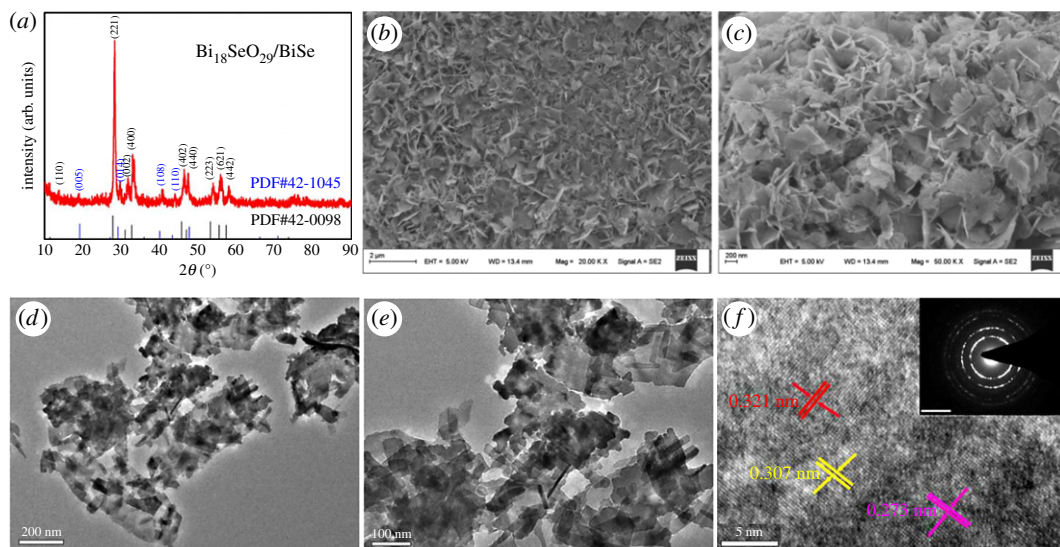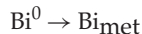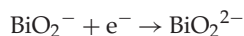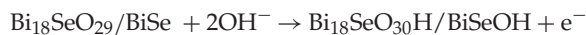
$$Bi^{3+} + 2OH^- \rightarrow Bi(OH)_2{}^+$$
$$2Bi(OH)_2{}^+ + 2OH^- \rightarrow Bi_2O_3 + 3H_2O$$
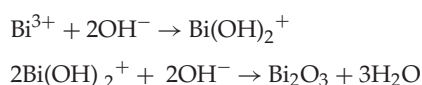
Figure 1. (*a*) XRD pattern of $Bi_{18}SeO_{29}$/BiSe nanosheets; (*b,c*) SEM and (*d,e*) TEM images of $Bi_{18}SeO_{29}$/BiSe nanosheets at various magnifications; (*f*) high-resolution TEM image of the $Bi_{18}SeO_{29}$/BiSe nanosheets.

$$Bi_2O_3 + 2OH^- \rightarrow 2BiO_2^- + H_2O$$

$$Bi_{18}SeO_{29}/BiSe + 2OH^- \rightarrow Bi_{18}SeO_{30}H/BiSeOH + e^-$$

$$BiO_2^- + e^- \rightarrow BiO_2^{2-}$$

$$BiO_2^{2-} + 2H_2O \rightarrow BiO_2^- + 4OH^- + Bi^0$$

$$Bi^0 \rightarrow Bi_{met}$$
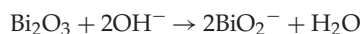
Here, Bi^0 are active atoms and Bi_{met} is the metal bismuth.

There are characteristic redox peaks of the electrode observed from -1 to $0\,V$ which correspond to the reversible intercalation/deintercalation of OH^- ions occurring in the $Bi_{18}SeO_{29}$/BiSe bulk and at the interface of $Bi_{18}SeO_{29}$/BiSe and electrolyte to increase the discharge time.

From the CV curve, we can see that the shape remains similar even at high scan rates, which indicates that the $Bi_{18}SeO_{29}$/BiSe electrode material has excellent capacitance behaviour. And at higher sweep rates, the higher/lower potentials the reduction and oxidation peak potentials move, because the ions may only be immersed in the surface of the material; however at a lower sweep rates, ions can be effectively diffused into the inner active sites. As the lower scan rates are provided for a longer period of time, the active site interacts with the ions better. So it is obvious that as the scan rate increases, the specific capacitance will be reduced. The various current density GCD curves of the $Bi_{18}SeO_{29}$/BiSe electrode are presented in figure 3*b*; the charge/discharge curve reveals the pseudocapacitance behaviour. In the discharge process, there is a kink in the curve, which is perhaps some of the untransformed Bi^0 oxidation platforms during the reduction process. These results are consistent with that consequence of the CV curves. As exhibited in figure 3*c*, the specific capacitances of the $Bi_{18}SeO_{29}$/BiSe electrode at various current densities of 0.5, 1, 2, 3, 5, 8 and 10 A g^{-1} are 471.3, 373, 331.2, 320.4, 307, 291.2 and 285 F g^{-1}, respectively. This indicates outstanding rate capability [44]. This phenomenon is also present in transition metal sulfides and oxides/hydroxides, which can be attributed to the diffusion effect [45,46]. To evaluate the cycling stability, the GCD cycling of $Bi_{18}SeO_{29}$/BiSe was observed at a current density of 2 A g^{-1} (figure 3*d*), which indicates that $Bi_{18}SeO_{29}$/BiSe has good cycling stability with about 68% capacitance retention after 5000 cycles in 2 M KOH electrolyte. This result makes $Bi_{18}SeO_{29}$/BiSe a promising candidate as an advanced electrode material for supercapacitor application.

3.2. Positive electrode

The $Co_{0.85}Se$ was characterized in detail. From the XRD pattern displayed in figure 4*a*, the diffraction peaks can be indexed to $Co_{0.85}Se$ with the hexagonal structure (JCPDS card no. 52-1008) readily. The pure phase and sharp peaks show that $Co_{0.85}Se$ has high crystallinity. The strong diffraction peaks at $2\theta = 33.3$,

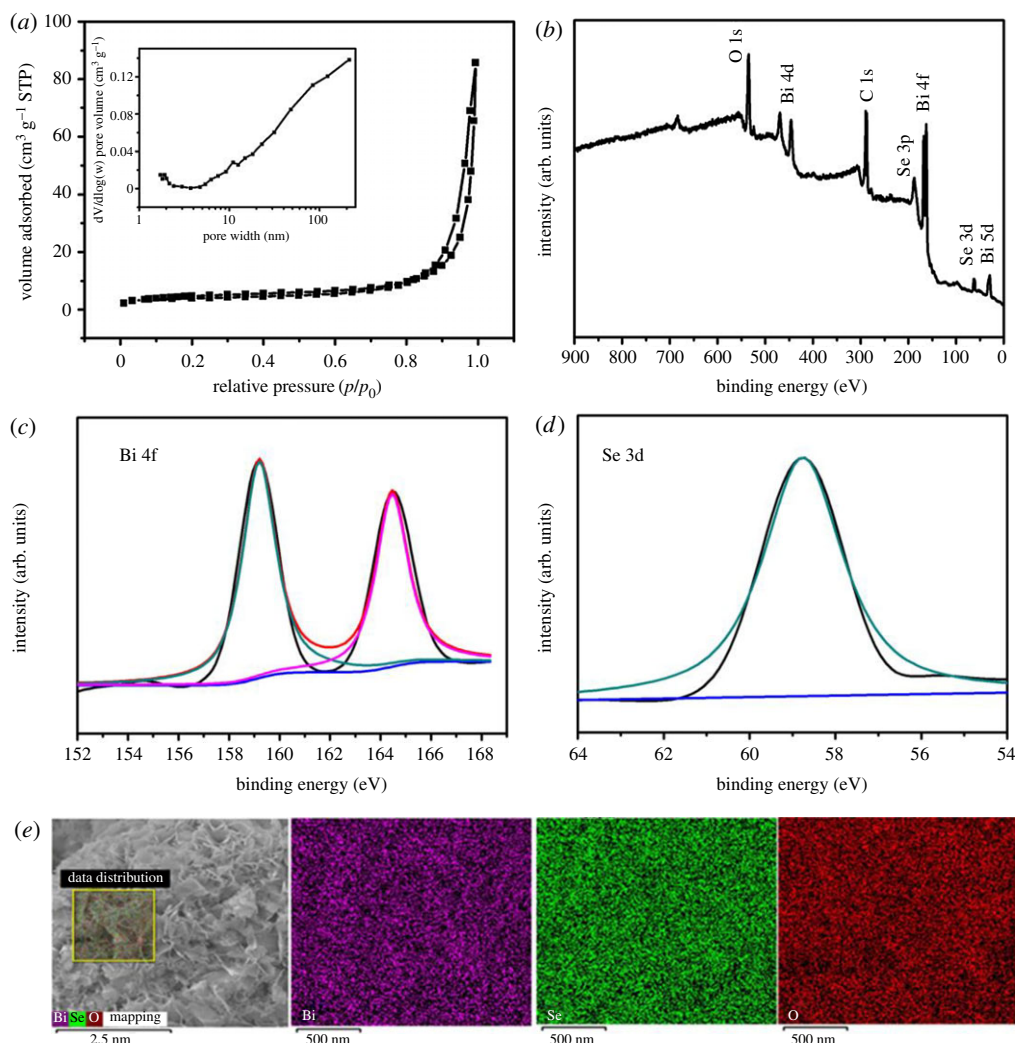**Figure 2.** (*a*) Nitrogen adsorption–desorption isotherms and (inset) pore size distribution of $Bi_{18}SeO_{29}$/BiSe. (*b*) XPS of $Bi_{18}SeO_{29}$/BiSe; (*c*) high-resolution XPS spectra of Bi 4f peak; (*d*) high-resolution XPS spectra of Se 3d peak and (*e*) the corresponding element mapping images (selected from the square region) for the bismuth, selenium and oxygen of $Bi_{18}SeO_{29}$/BiSe nanosheets.

44.7 and 50.6 unequivocally correspond to the (101), (102), and (110) planes of $Co0.85Se$, respectively. The morphology characteristic features of the $Co_{0.85}Se$ sample were analysed via SEM. The SEM images (figure 4*b*) display a particular flower-like morphology, which is combined with the subunits of the nanosheet. The high-resolution SEM image (figure 4*c*) clearly shows a flower-like 3D microstructure, which could facilitate penetration of the electrolyte into the material and also increase the electrochemical reactions of the active sites. Further, the microstructure was also described by the corresponding TEM and high-resolution TEM images. As can be seen in figure 4*d–f*, $Co_{0.85}Se$ is constituted of many thin nanosheets, which are consistent with those in SEM. From figure 4*f*, well-defined lattice fringes are clearly seen with an interplanar spacing of 0.27 nm. This corresponds to the separation between (101) lattice planes of $Co_{0.85}Se$. In the SAED pattern shown in the inset of figure 4*f*, the diffraction rings could be easily indexed to $Co_{0.85}Se$ with the hexagonal (101), (102), (110) and (103) planes from inside to outside, suggesting that the nanosheet is of polycrystalline nature [31], which shows good agreement with the XRD pattern and can be indexed to the structure.

The specific surface area and pore size distribution of $Co_{0.85}Se$ were examined by N_2 adsorption–desorption measurements. As displayed in figure 5*a* and inset, at a relative pressure of 0.9–0.99, the apparent N_2 adsorption and the hysteresis loop indicate the coexistence of a minor fraction of mesopores/macropores, which is mainly due to the 3D voids between interconnected particles [47]. The specific surface area of $Co_{0.85}Se$ calculated by the multiple points BET method is $73.3 \, m^2 \, g^{-1}$, which is larger than that of the previously reported $Co_{0.85}Se$ electrode materials; Gong *et al*. described a specific
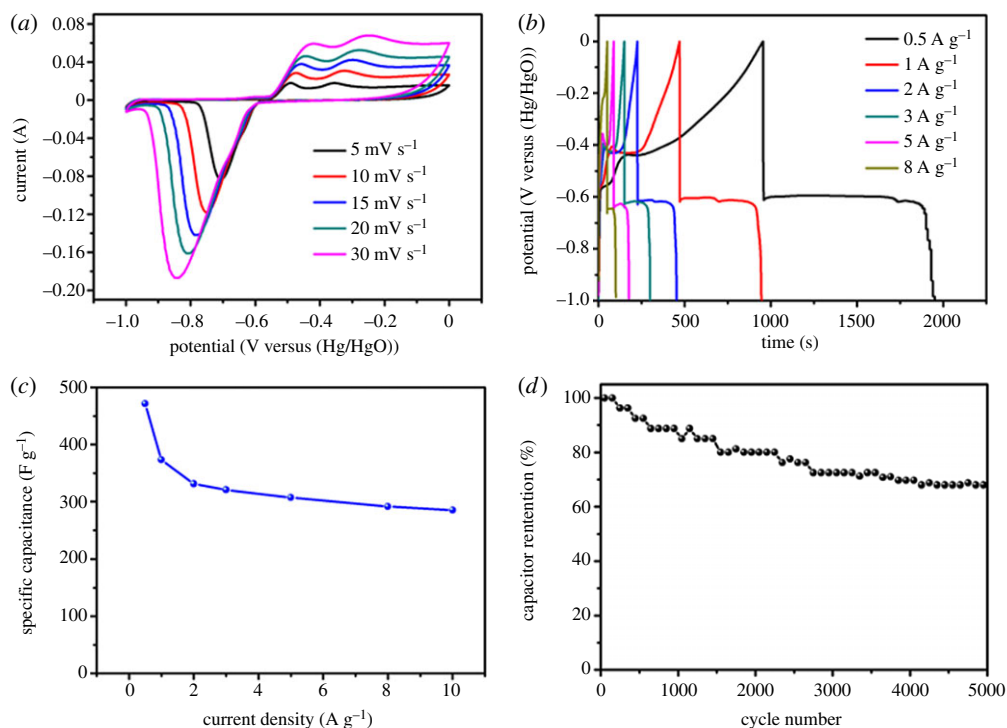
Figure 3. The electrochemical properties of synthesized $Bi_{18}SeO_{29}/BiSe$ electrode materials via a three-electrode system: (*a*) CV curves at different scan rates; (*b*) GCD curves with various current densities; (*c*) with the increase in current density the changes in specific capacitance changes; and (*d*) cycling stability of the $Bi_{18}SeO_{29}/BiSe$ electrode material at a current density of 2 A g^{-1}.

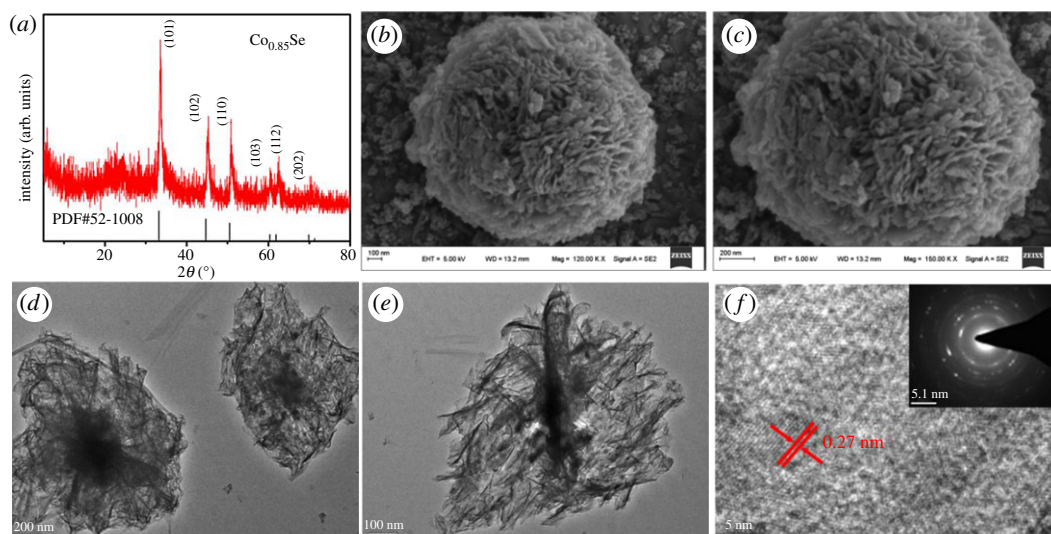**Figure 4.** (*a*) XRD pattern of $Co_{0.85}Se$ nanosheets; (*b,c*) SEM and (*d,e*) TEM images of $Co_{0.85}Se$ nanosheets at various magnifications; (*f*) high-resolution TEM image of the $Co_{0.85}Se$ nanosheets.

surface area of 26.44 m^2 g^{-1} [48] and Yang *et al*. described 59 m^2 g^{-1} [31]. A mass of the 3D porous structure will favour the penetration of electrolyte and the rapid transmission of electrons, which will improve the electrochemical properties of the $Co_{0.85}Se$ electrode material.

The XPS and EDS techniques were used to evaluate the surface valence state information and the chemical element compositions of $Co_{0.85}Se$ (figure 5*b–d*), mainly exhibiting the Se 3d and Co 2p peaks. Figure 5*b* shows the Co $2p_{3/2}$, $2p_{1/2}$ and two satellite peaks (marked as 'sat.'). The Co^{3+} $2p_{3/2}$, Co^{2+} $2p_{3/2}$ and Co^{2+} $2p_{1/2}$ are corresponding to binding energies of 779.0, 780.8 and 797.2 eV, respectively.
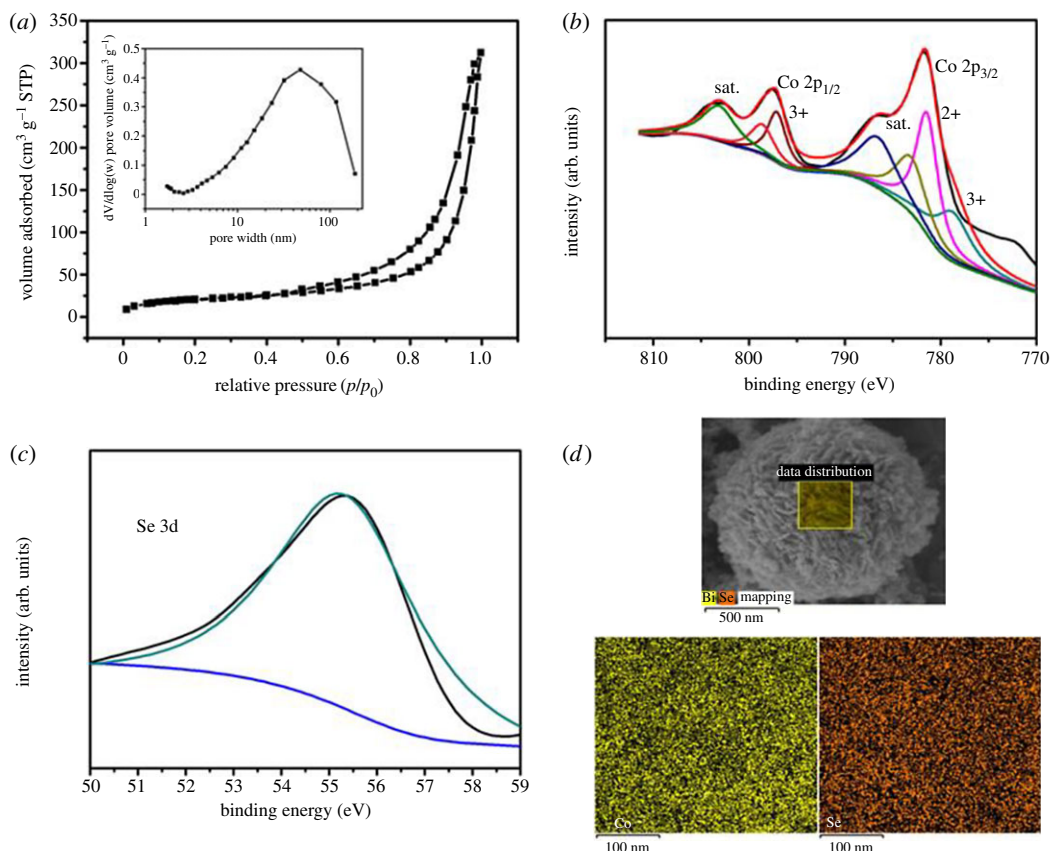
Figure 5. (*a*) Nitrogen adsorption–desorption isotherms and (inset) pore size distribution of $Co_{0.85}Se$; (*b*) high-resolution XPS spectra of $Co_{2p1/2}$ and $Co_{2p3/2}$ peak; (*c*) high-resolution XPS spectra of Se 3d peak; and (*d*) the corresponding element mapping images (selected from the square region) for the $Co_{0.85}Se$ nanosheets.

The two spin–orbit doublets characteristic of Co^{2+} and Co^{3+} are considered and consistent with the previously reported values [37]. Furthermore, figure 5*c* clearly displays the core region of the binding energy of 55.4 eV corresponding to the Se 3d spectrum, and this approached the reported value [49]. The results show that the synthesized $Co_{0.85}Se$ electrode material consisted of Co^{2+}, Co^{3+} and Se^2, which is consistent with the formula $Co_{0.85}Se$. Furthermore, the $Co_{0.85}Se$ electrode material is synthesized by element mapping images of cobalt and selenium in figure 5*d*, in which it is obvious that the elemental distributions are very uniform.

Electrochemical behaviours of the $Co_{0.85}Se$ electrode material were investigated by CV and GCD measurements with 2 M KOH at a voltage window between -0.1 and 0.6 V (versus Hg/HgO) in a standard three-electrode system. From figure 6*a*, it is clear that the area surrounded by the CV curve of $Co_{0.85}Se$ exhibits two pairs redox peaks, which might be attributed to standard Faradaic pseudocapacitance behaviour. The two pairs ascribed to the reversible redox reaction can occur according to [50]
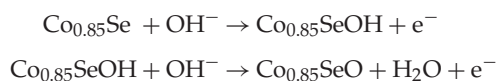
$$Co_{0.85}Se + OH^- \rightarrow Co_{0.85}SeOH + e^-$$

$$Co_{0.85}SeOH + OH^- \rightarrow Co_{0.85}SeO + H_2O + e^-$$

Figure 6*a* describes the typical CV curves of the $Co_{0.85}Se$ nanosheets at various scan rates from 5 to $30 \, mV \, s^{-1}$, from which, even at a high scan rate of $30 \, mV \, s^{-1}$, two pairs of reversible redox peaks can be obviously observed. In addition, due to the presence of polarization, with the increase of the scan rate the position of the redox peak gradually changes [50]. The GCD test results are presented in figure 6*b* to analyse the charge storage capacity of the electrode material. Because the redox reaction occurs at the electrode interface by the desorption and adsorption of the hydroxyl ion in the alkaline electrolyte [51], it is obvious that each charge–discharge curve indicates pseudocapacitive performance at current densities from 0.5 to $8 \, A \, g^{-1}$, and deviates from the EDLC linear curve. All of the charge–discharge curves
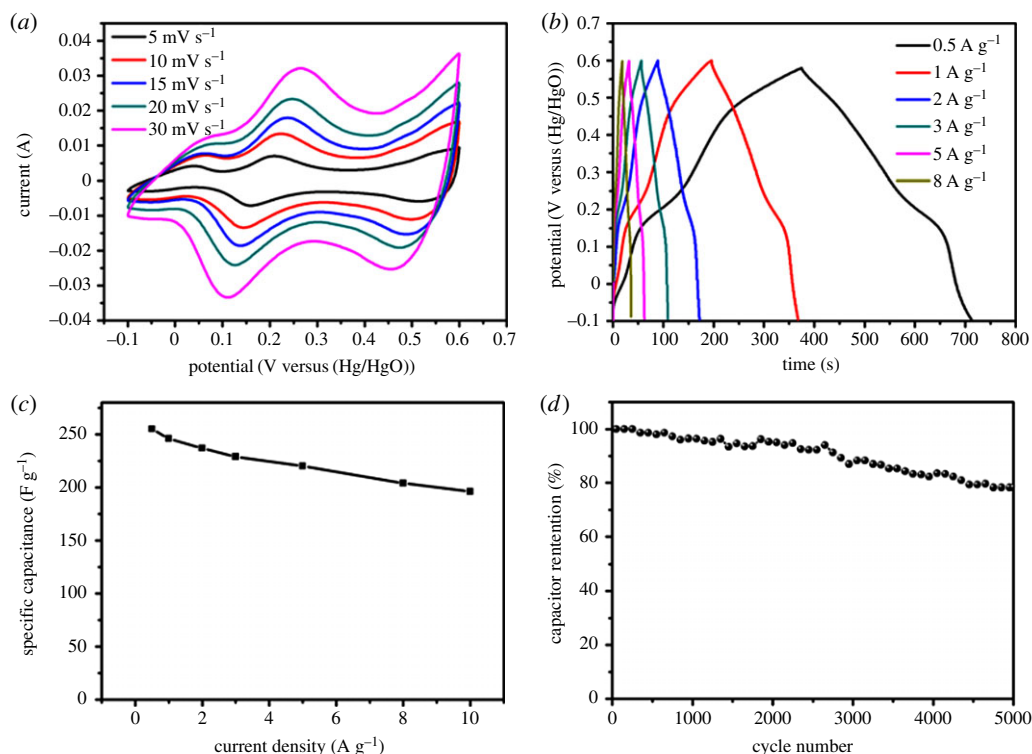
Figure 6. The electrochemical properties of synthesized electrode $Co_{0.85}Se$ materials in a three-electrode system: (*a*) CV curves with various scan rates; (*b*) GCD curves at different current densities; (*c*) the change of specific capacitance with the increase in current density; and (*d*) cycling stability of $Co_{0.85}Se$ electrode material at a current density of $2\,A\,g^{-1}$.

are almost symmetrical, which reveals that $Co_{0.85}Se$ has excellent capacitive behaviour. As displayed in figure 6*c*, the specific capacitance of $Co_{0.85}Se$ is calculated to be 255, 246, 237, 229, 220, 204 and $196\,F\,g^{-1}$ at various current densities from 0.5 to $10\,A\,g^{-1}$, exhibiting an outstanding rate capability. The stability of the $Co_{0.85}Se$ electrode material was tested using the charging and discharge technique at a current density of $2\,A\,g^{-1}$. Finally, it is seen to retain about 78% of its initial capacitance after 5000 cycles, indicating that the $Co_{0.85}Se$ positive electrode material possesses outstanding cycling stability.

3.3. Asymmetric supercapacitor

In practical applications, to further evaluate the electrochemical performance of the electrode materials, we assembled an ASC, in which $Bi_{18}SeO_{29}/BiSe$ and $Co_{0.85}Se$ worked as the negative and positive electrode materials in 2 M KOH electrolyte. To ensure the electrochemical stability of the two-electrode cell with the acquired optimized potential window, the CVs of $Bi_{18}SeO_{29}/BiSe$ (black) and the $Co_{0.85}Se$ (red) were tested in 2 M KOH electrolyte at $30\,mV\,s^{-1}$. As displayed in figure 7*a*, the stable potential range of $Co_{0.85}Se$ is between 0 and 0.6 V and the capacitive behaviour of $Bi_{18}SeO_{29}/BiSe$ is between -1 and 0 V. Therefore, the operating cell voltage can be optimized to 1.6 V in 2 M KOH aqueous solution for the ASC of $Bi_{18}SeO_{29}/BiSe//Co_{0.85}Se$ (figure 7*b*). In the design of the asymmetric cell, the balance of the charge stored between the positive and negative electrodes was necessary and it was calculated by equations (2.2) and (2.3). The CV curves of the $Bi_{18}SeO_{29}/BiSe//Co_{0.85}Se$ ASC device were analysed at various scan rates (between 10 and $100\,mV\,s^{-1}$) with an operating voltage of 1.6 V. Figure 7*b* clearly shows that three pairs of redox peaks can be attributed to the redox reactions of $Bi_{18}SeO_{29}/BiSe$ and $Co_{0.85}Se$ in 2 M KOH electrolyte. In addition, all curves show similar shapes; meanwhile changes in anode and cathode peaks even at high scan rate of $100\,mV\,s^{-1}$ of the ASC are small, indicating outstanding reversibility of the ASC. Figure 7*c* exhibits the GCD curves of the $Bi_{18}SeO_{29}/BiSe//Co_{0.85}Se$ ASC device at different current densities (ranging from 0.5 to $8\,A\,g^{-1}$), and this proves the coexistence of the oxidation of anions and surface adsorption of ions in this ASC device. An advanced Ragone diagram (energy density versus power density) of the $Bi_{18}SeO_{29}/BiSe//Co_{0.85}Se$ ASC device is obtained from the GCD data (figure 7*c*) as revealed in figure 7*d*, according to equations (2.5) and (2.6). The device exhibits a high energy density
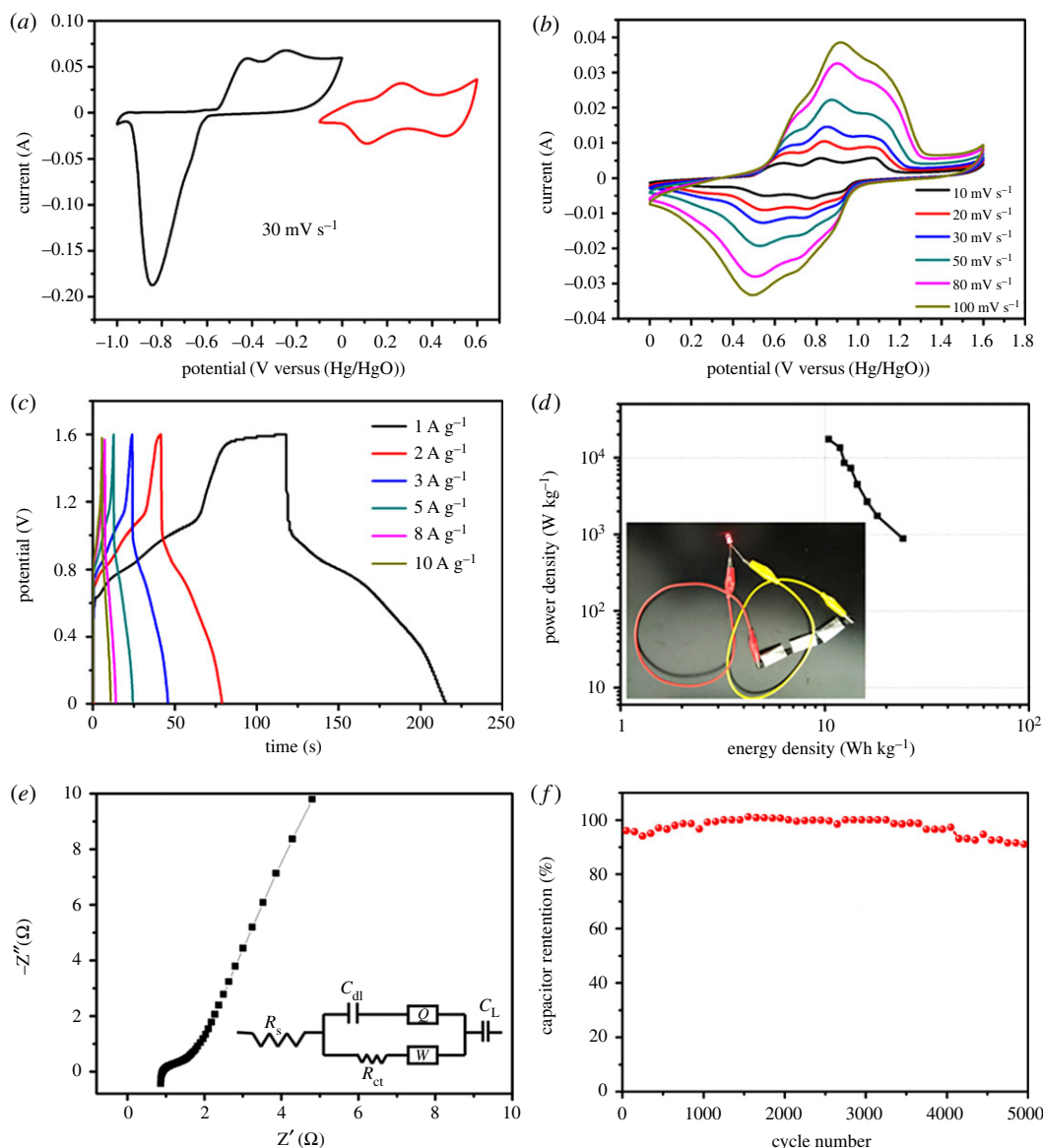
Figure 7. (*a*) CV curves of the $Bi_{18}SeO_{29}/BiSe$ and $Co_{0.85}Se$ electrodes via a two-electrode cell at 30 mV s^{-1} in 2 M KOH; (*b*) CV curves of the ASC device with different scan rates; (*c*) GCD curves at different current densities; (*d*) Ragone plot related to energy and power densities of the ASC; (*e*) Nyquist plot of the ASC (inset shows the equivalent circuit model); (*f*) cycling stability of the $Bi_{18}SeO_{29}/BiSe//Co_{0.85}Se$ ASC in a two-electrode cell.

that reaches 24.2 Wh kg^{-1} at an outstanding power density of 871.2 W kg^{-1} at a current density of 1 A g^{-1}. Even when the current density is as high as 15 A g^{-1}, the energy density still remains at 11.9 Wh kg^{-1} with an excellent power density of 13 387.5 W kg^{-1}. The energy density of the $Bi_{18}SeO_{29}/BiSe//Co_{0.85}Se$ ASC device is shown in figure 7*d*. To verify the feasibility of energy supply for the $Bi_{18}SeO_{29}/BiSe//Co_{0.85}Se$ ASC, the three-tandem cell group can light up a red light-emitting diode (figure 7*d*, inset). Therefore, the excellent high energy density indicates that it has great potential as a supercapacitor.

The facilitated ion or electron transport kinetics of the $Bi_{18}SeO_{29}/BiSe//Co_{0.85}Se$ ASC device was investigated by EIS. The Nyquist plot of the ASC device and the corresponding equivalent circuit are shown in figure 7*e* and in the inset of figure 7*e*, respectively. It consists of three different parts at a distinct frequency range: high frequencies, an unfinished semicircular part; the middle frequencies, an inclined portion in the curve (about 45°); and the low frequencies, the linear part. The high frequency of the real axis intercept indicates the internal resistance (R_s), which is the sum of the large amount of electrolyte resistance, the contact resistance of the electrode/electrolyte interface and the intrinsic resistance of the electrode active material [52]. The charge transfer resistance (R_{ct}) is the diameter of the

semicircle which is related to the charge transfer at the electrode/electrolyte interface and thus produced a Faraday reaction [46]; in the middle frequencies, the 45° slope of the line is called Warburg impedance (Z_w), which is caused by the diffusion process of the electrolyte [53]. Moreover, C_L and C_{dl} represent the limit capacitance and the double-layer capacitance [54]. As can be seen from the fitted results, a $Bi_{18}SeO_{29}/BiSe//Co_{0.85}Se$ ASC device not only has a low R_s ($0.88\,\Omega\,cm^2$), but also possesses a small R_{ct} ($1.87\,\Omega\,cm^2$), as well as a low Warburg resistance ($0.017\,\Omega\,cm^2$). The values demonstrate that the electrolyte permeation and ion diffusion into the pore structure are very easy, and these values may belong to electrode materials with special structure. On the one hand, $Bi_{18}SeO_{29}/BiSe$ is an ultrathin nanosheet, and it can provide an efficient pathway for charge transportation; on the other hand, $Co_{0.85}Se$ material has a 3D high surface area, for adsorbing ions to provide abundant electrical active sites. These results can facilitate transport of the electrolyte. The cyclic stability of the $Bi_{18}SeO_{29}/BiSe//Co_{0.85}Se$ ASC device is evaluated by the GCD process with a current density of $2\,A\,g^{-1}$ after 5000 cycles and an operating voltage of 0–1.6 V (figure 7f). Owing to the full activation of the $Bi_{18}SeO_{29}/BiSe$ and $Co_{0.85}Se$ materials, the specific capacitance increases at the beginning, and even after 1500 cycles, the degradation of the active material was not observed with maintenance of 100% initial capacity. Thus, excellent cycling performance is shown. Finally, the ASC device shows only a slight decrease in specific capacitance (about 93% of the initial specific capacitance retention after 5000 cycles), indicating excellent cycle stability. The above results mean that the high-performance ASC with excellent stability may be a candidate for energy storage devices in future electronic application.

4. Conclusion

In summary, the negative $Bi_{18}SeO_{29}/BiSe$ and positive $Co_{0.85}Se$ electrode materials are prepared through a simple one-step hydrothermal method without any template and surfactant. $Bi_{18}SeO_{29}/BiSe$ and $Co_{0.85}Se$ have high specific capacitance ($471.3\,F\,g^{-1}$ and $255\,F\,g^{-1}$ at $0.5\,A\,g^{-1}$), high conductivity, outstanding cycling stability, as well as good rate capability. The all-pseudocapacitive electrodes fabricated $Bi_{18}SeO_{29}/BiSe//Co_{0.85}Se$ ASC device has excellent electrochemical performance with a good cycling stability (93% capacitance retention after 5000 cycles at a current density of $2\,A\,g^{-1}$) and high energy density (about $24.2\,Wh\,kg^{-1}$) as well as high power density (about $871.2\,W\,kg^{-1}$) in aqueous electrolyte at a wide voltage window of 0–1.6 V. The results demonstrate that the electrode material preparation approach is easy and also the resulting ASC is promising as an energy-storage device.

References

1. Wei W, Cui X, Chen W, Ivey DG. 2011 Manganese oxide-based materials as electrochemical supercapacitor electrodes. *Chem. Soc. Rev.* **40**, 1697–1721. (doi:10.1039/C0CS00127A)

2. Li Y, Xu J, Feng T, Yao Q, Xie J, Xia H. 2017 Fe₂O₃ nanoneedles on ultrafine nickel nanotube arrays as efficient anode for high-performance asymmetric supercapacitors. *Adv. Funct. Mater.* **27**, 1606728. (doi:10.1002/adfm.201606728)

3. Yuan C, Li J, Hou L, Zhang X, Shen L, Lou XW. 2012 Ultrathin mesoporous NiCo₂O₄ nanosheets supported on Ni foam as advanced electrodes for

supercapacitors. *Adv. Funct. Mater.* **22**, 4592–4597. (doi:10.1002/adfm.201200994)

4. Jiang H, Ma J, Li C. 2012 Mesoporous carbon incorporated metal oxide nanomaterials as supercapacitor electrodes. *Adv. Mater.* **24**, 4197–4202. (doi:10.1002/adma.201104942)

5. Wang G, Zhang L, Zhang J. 2012 A review of electrode materials for electrochemical supercapacitors. *Chem. Soc. Rev.* **41**, 797–828. (doi:10.1039/C1CS15060J)

6. Augustyn V, Simon P, Dunn B. 2014 Pseudocapacitive oxide materials for high-rate

electrochemical energy storage. *Energy Environ. Sci.* **7**, 1597–1614. (doi:10.1039/C3EE44164D)

7. Hong X, Hui KS, Zeng Z, Hui KN, Zhang L, Mo M, Li M. 2014 Hierarchical nitrogen-doped porous carbon with high surface area derived from endothelium corneum gigeriae galli for high-performance supercapacitor. *Electrochim. Acta* **130**, 464–469. (doi:10.1016/j.electacta.2014.03.015)

8. Chen PC, Shen G, Shi Y, Chen H, Zhou C. 2010 Preparation and characterization of flexible asymmetric supercapacitors based on transition-metal-oxide nanowire/single-walled

carbon nanotube hybrid thin-film electrodes. *ACS Nano* **4**, 4403–4411. (doi:10.1021/nn100856y)

9. Tian Z, Dou H, Zhang B, Fan W, Wang X. 2017 Three-dimensional graphene combined with hierarchical CuS for the design of flexible solid-state supercapacitors. *Electrochim. Acta* **237**, 109–118. (doi:10.1016/j.electacta.2017.03.207)

10. Zhao C, Shao X, Zhu Z, Zhao C, Qian X. 2017 One-pot hydrothermal synthesis of RGO/FeS composite on Fe foil for high performance supercapacitors. *Electrochim. Acta* **246**, 497–506. (doi:10.1016/j.electacta.2017.06.090)

11. Iqbal MF, Hassan MU, Ashiq MN, Iqbal S, Bibi N, Parveen B. 2017 High specific capacitance and energy density of synthesized graphene oxide based hierarchical Al_2S_3 nanorambutan for supercapacitor applications. *Electrochim. Acta* **246**, 1097–1103. (doi:10.1016/j.electacta.2017.06.123)

12. Yang H, Xu H, Li M, Zhang L, Huang Y, Hu X. 2016 New off-on sensor for captopril sensing based on photoluminescent MoO x quantum dots. *ACS Appl. Mater. Inter.* **8**, 1774–1779. (doi:10.1021/acsomega.7b00088)

13. Borysiewicz MA, Ekielski M, Ogorzałek Z, Wzorek M, Kaczmarski J, Wojciechowski T. 2017 Highly transparent supercapacitors based on ZnO/MnO_2 nanostructures. *Nanoscale* **9**, 7577–7587. (doi:10.1039/C7NR01320E)

14. Ke Q, Guan C, Zhang X, Zheng M, Zhang Y, Cai Y, Zhang H, Wang J. 2017 Surface-charge-mediated formation of H-TiO_2@Ni(OH)$_2$ heterostructures for high-performance supercapacitors. *Adv. Mater.* **29**, 1604164. (doi:10.1002/adma.201604164)

15. Pang H, Li X, Zhao Q, Xue H, Lai WY, Hu Z, Huang W. 2017 One-pot synthesis of heterogeneous Co_3O_4-nanocube/Co(OH)$_2$-nanosheet hybrids for high-performance flexible asymmetric all-solid-state supercapacitors. *Nano Energy* **35**, 138–145. (doi:10.1016/j.nanoen.2017.02.044)

16. Shen J, Wu J, Pei L, Rodrigues M-TF, Zhang Z, Zhang F, Zhang X, Ajayan PM, Ye M. 2016 CoNi$_2$S$_4$-graphene-2D-MoSe$_2$ as an advanced electrode material for supercapacitors. *Adv. Energy. Mater.* **6**, 1600341. (doi:10.1002/aenm.201600341)

17. Hong X, Zhang B, Murphy E, Zou J, Kim F. 2017 Three-dimensional reduced graphene oxide/polyaniline nanocomposite film prepared by diffusion driven layer-by-layer assembly for high-performance supercapacitors. *J. Power Sources* **343**, 60–66. (doi:10.1016/j.jpowsour.2017.01.034)

18. Gong MX, Li S, Lee PS. 2017 A fiber asymmetric supercapacitor based on FeOOH/PPy on carbon fibers as an anode electrode with high volumetric energy density for wearable applications. *Nanoscale* **9**, 10 794–10 801. (doi:10.1039/C7NR02896B)

19. Chen H, Jiang J, Zhang L, Xia D, Zhao Y, Guo D, Qi T, Wan H. 2014 In situ growth of NiCo$_2$S$_4$ nanotube arrays on Ni foam for supercapacitors: maximizing utilization efficiency at high mass loading to achieve ultrahigh areal pseudocapacitance. *J. Power Sources* **254**, 249–257. (doi:10.1016/j.jpowsour.2013.12.092)

20. Zhang X, Zhang J, Zhao J, Pan B, Kong M, Chen J, Xie Y. 2012 Half-metallic ferromagnetism in synthetic Co$_9$Se$_8$ nanosheets with atomic thickness. *J. Am. Chem. Soc.* **134**, 11 908–11 911. (doi:10.1021/ja3046603)

21. Balasingam SK, Lee JS, Jun Y. 2015 Few-layered MoSe$_2$ nanosheets as an advanced electrode material for supercapacitors. *Dalton Trans.* **44**, 15 491–15 498. (doi:10.1039/C5DT01985K)

22. Wang X, Liu B, Wang Q, Song W, Hou X, Chen D, Cheng Y, Shen G. 2013 Three-dimensional hierarchical GeSe$_2$ nanostructures for high performance flexible all-solid-state supercapacitors. *Adv. Mater.* **25**, 1479–1486. (doi:10.1002/adma.201204063)

23. Choi J, Jin J, Jung IG, Kim JM, Kim HJ, Son SU. 2011 SnSe$_2$ nanoplate-graphene composites as anode materials for lithium ion batteries. *Chem. Commun.* **47**, 5241–5243. (doi:10.1039/C1CC10317B)

24. Tang C, Pu Z, Liu Q, Asiri AM, Sun X, Luo Y, He Y. 2015 *In situ* growth of NiSe nanowire film on nickel foam as an electrode for high-performance supercapacitors. *ChemElectroChem* **2**, 1903–1907. (doi:10.1002/celc.201500285)

25. Yang J, Yuan Y, Wang W, Tang H, Ye Z, Lu J. 2017 Interconnected Co$_{0.85}$Se nanosheets as cathode materials for asymmetric supercapacitors. *J. Power Sources* **340**, 6–13. (doi:10.1016/j.jpowsour.2016.11.061)

26. Watanabe M, Thomas ML, Zhang S, Ueno K, Yasuda T, Dokko K. 2017 Application of ionic liquids to energy storage and conversion materials and devices. *Chem. Rev.* **117**, 7190–7239. (doi:10.1021/acs.chemrev.6b00504)

27. Chaudoy V, Van FT, Deschamps M, Ghamouss F. 2017 Ionic liquids in a polyethylene oxide cross-linked gel polymer as an electrolyte for electrical double layer capacitor. *J. Power Sources* **342**, 872–878. (doi:10.1016/j.jpowsour.2016.12.097)

28. Pinna N, Niederberger M. 2008 Surfactant-free nonaqueous synthesis of metal oxide nanostructures. *Angew. Chem., Int. Ed.* **47**, 5292–5304. (doi:10.1002/anie.200704541)

29. Niederberger M, Pinna N. 2009 *Metal oxide nanoparticles in organic solvents: synthesis, formation, assembly and application*. London, UK: Springer.

30. Bullen CR, Mulvaney P. 2004 Nucleation and growth kinetics of CdSe nanocrystals in octadecene. *Nano Lett.* **4**, 2303–2307. (doi:10.1021/nl0496724)

31. Ludi B, Süess MJ, Werner IA, Niederberger M. 2012 Mechanistic aspects of molecular formation and crystallization of zinc oxide nanoparticles in benzyl alcohol. *Nanoscale* **4**, 1982–1995. (doi:10.1039/C1NR11557J)

32. Peng H, Ma G, Sun K, Mu J, Zhang Z, Lei Z. 2014 Formation of carbon nanosheets via simultaneous activation and catalytic carbonization of macroporous anion-exchange resin for supercapacitors application. *ACS Appl. Mater. Interfaces* **6**, 20 795–20 803. (doi:10.1021/am505066v)

33. Li HB, Yu MH, Wang FX, Liu P, Liang Y, Xiao J, Wang CX, Tong YX, Yang GW. 2013 Amorphous nickel hydroxide nanospheres with ultrahigh capacitance and energy density as electrochemical pseudocapacitor materials. *Nat. Commun.* **4**, 1894. (doi:10.1038/ncomms2932)

34. Ma G, Zhang Z, Sun K, Feng E, Peng H, Zhou X, Lei Z. 2016 High-performance aqueous asymmetric supercapacitor based on K$_{0.3}$WO$_3$ nanorods and nitrogen-doped porous carbon. *J. Power Sources* **330**, 219–230. (doi:10.1016/j.jpowsour.2016.09.022)

35. Dupont M, Hollenkamp AF, Donne SW. 2013 Electrochemically active surface area effects on the performance of manganese dioxide for electrochemical capacitor applications. *Electrochim. Acta* **104**, 140–147. (doi:10.1016/j.electacta.2013.04.007)

36. Abdolmaleki A, Kazerooni H, Gholivand MB, Heydari H, Pendashteh A. 2015 Facile electrostatic coprecipitation of f-SWCNT/Co$_3$O$_4$ nanocomposite as supercapacitor material. *Ionics* **2**, 515–523. (https://link.springer.com/article/10.1007/s11581-014-1173-5)

37. Vonlanthen D, Lazarev P, See KA, Wudl F, Heeger AJ. 2014 A stable polyaniline-benzoquinone-hydroquinone supercapacitor. *Adv. Mater.* **26**, 5095–5100. (doi:10.1002/adma.201400966)

38. Wagner CD, Riggs WM, Davis LE, Moulder JF, Mouilenberg GE (eds). 1978 *Handbook of X-ray photoelectron spectroscopy*. Eden Prairie, MN: Perkin-Elmer Corporation.

39. Fan H, Wang G, Hu L. 2009 Infrared, Raman and XPS spectroscopic studies of Bi$_2$O$_3$-B$_2$O$_3$-Ga$_2$O$_3$ glasses. *Solid State Sci.* **11**, 2065–2070. (doi:10.1016/j.solidstatesciences.2009.09.007)

40. Wenkin M, Ruiz P, Delmon B, Devillers M. 2002 The role of bismuth as promoter in Pd–Bi catalysts for the selective oxidation of glucose to gluconate. *J. Mol. Catal. A* **180**, 141–159. (doi:10.1016/S1381-1169(01)00421-6)

41. Zheng FL, Li GR, Qu YN, Wang ZL, Su CY, Tong YX. 2010 Synthesis of hierarchical rippled Bi$_2$O$_3$ nanobelts for supercapacitor applications. *Chem. Commun.* **46**, 5021–5023. (doi:10.1039/C002126A)

42. Yuan D, Zeng J, Kristian N, Wang Y, Wang X. 2009 Bi$_2$O$_3$ deposited on highly ordered mesoporous carbon for supercapacitors. *Electrochem. Commun.* **11**, 313–317. (doi:10.1016/j.elecom.2008.11.041)

43. Wang SX, Jin CC, Qian WJ. 2014 Bi$_2$O$_3$ with activated carbon composite as a supercapacitor electrode. *J. Alloys Compd.* **615**, 12–17. (doi:10.1016/j.jallcom.2014.06.149)

44. Fan Z, Yan J, Wei T, Zhi L, Ning G, Li T, Wei F. 2011 Asymmetric supercapacitors based on graphene/MnO$_2$ and activated carbon nanofiber electrodes with high power and energy density. *Adv. Funct. Mater.* **21**, 2366–2375. (doi:10.1002/adfm.201100058)

45. Nagaraju G, Raju GSR, Ko YH, Yu JS. 2016 Hierarchical Ni-Co layered double hydroxide nanosheets entrapped on conductive textile fibers: a cost-effective and flexible electrode for high-performance pseudocapacitors. *Nanoscale* **8**, 812–825. (doi:10.1039/C5NR05643H)

46. Peng S *et al.* 2014 Hollow spheres: MS$_2$ (M = Co and Ni) hollow spheres with tunable interiors for high-performance supercapacitors and photovoltaics (Adv. Funct. Mater. 15/2014). *Adv. Funct. Mater.* **24**, 2154. (doi:10.1002/adfm.201470095)

47. Chang J, Gao Z, Zhao W, Guo L, Chu M, Tang Y, Wu D, Xu F, Jiang K. 2016 Nitrogen doped microporous carbons with tunable and selective performances in supercapacitor and heterogeneous catalysis. *Electrochim. Acta* **190**, 912–922. (doi:10.1016/j.electacta.2015.12.113)

48. Gong C, Huang M, Zhou P, Sun Z, Fan L, Lin J, Wu J. 2016 Mesoporous Co$_{0.85}$Se nanosheets supported on Ni foam as a positive electrode material for asymmetric supercapacitor. *App. Surf. Sci.*

362, 469–476. (doi:10.1016/j.apsusc.2015.11.194)

49. Wagner C, Riggs W, Davis L, Moulder J, Muilenberg G. 1979 *Handbook of X-ray photoelectron spectroscopy*. Eden Prairie, MN: Perkin-Elmer Corporation, Physical Electronics Division.

50. Banerjee A, Bhatnagar S, Upadhyay KK, Yadav P, Ogale S. 2014 Hollow $Co_{0.85}$Se nanowire array on carbon fiber paper for high rate pseudocapacitor. *ACS Appl. Mater. Interfaces* **6**, 18 844–18 852. (doi:10.1021/am504333z)

51. Wu C, Wang X, Ju B, Zhang X, Jiang L, Wu H. 2012 Supercapacitive behaviors of activated mesocarbon microbeads coated with polyaniline. *Int. J. Hydrog. Energy* **37**, 14 365–14 372. (doi:10.1016/j.ighydene.2012.07.087)

52. Peng S, Li L, Wu HB, Madhavi S, Lou XW. 2015 Controlled growth of $NiMoO_4$ nanosheet and nanorod arrays on various conductive substrates as advanced electrodes for asymmetric supercapacitors. *Adv. Energy Mater.* **5**, 1401172. (doi:10.1002/aenm.201401172)

53. Liu J, Jiang J, Bosman M, Fan HJ. 2012 Three-dimensional tubular arrays of MnO_2-NiO nanoflakes with high areal pseudocapacitance. *J. Mater. Chem.* **22**, 2419–2426. (doi:10.1039/C1JM14804D)

54. Zhang C, Xie L, Song W, Wang J, Sun G, Li K. 2013 Electrochemical performance of asymmetric supercapacitor based on Co_3O_4/AC materials. *J. Electroanal. Chem.* **706**, 1–6. (doi:10.1016/j.jelechem.2013.07.032)